Probing model tumor interfacial properties using piezoelectric cantilevers

Hakki Yegingil,[1] Wan Y. Shih,[2] and Wei-Heng Shih[1]

[1]*Department of Materials Science and Engineering, Drexel University, Philadelphia, Pennsylvania 19104, USA*
[2]*School of Biomedical Engineering, Science, and Health Systems, Drexel University, Philadelphia, Pennsylvania 19104, USA*

Invasive malignant breast cancers are typically branchy and benign breast tumors are typically smooth. It is of interest to characterize tumor branchiness (roughness) to differentiate invasive malignant breast cancer from noninvasive ones. In this study, we examined the shear modulus (G) to elastic modulus (E) ratio, G/E, as a quantity to describe model tumor interfacial roughness using a piezoelectric cantilever capable of measuring both tissue elastic modulus and tissue shear modulus. The piezoelectric cantilever used had two lead zirconate titanate layers to facilitate all-electrical elastic (shear) modulus measurements using one single device. We constructed model tissues with tumors by embedding one-dimensional (1D) corrugated inclusions and three-dimensional (3D) spiky-ball inclusions made of modeling clay in gelatin. We showed that for smooth inclusions, G/E was 0.3 regardless of the shear direction. In contrast, for a 1D corrugated rough inclusion G/E was 0.3 only when the shear was parallel to corrugation and G/E increased with an increasing angle between the shear direction and the corrugation. When the shear was perpendicular to corrugation, G/E became >0.7. For 3D isotropic spiky-ball inclusions we showed that the G/E depended on the degree of the roughness. Using the ratio s/r of the spike length (s) to the overall inclusion radius (r) as a roughness parameter, we showed that for inclusions with s/r larger than or equal to 0.28, the G/E ratio over the inclusions was larger than 0.7 whereas for inclusions with s/r less than 0.28, the G/E decreased with decreasing s/r to around 0.3 at s/r $=0$. In addition, we showed that the depth limit of the G/E measurement is twice the width of the probe area of the piezoelectric cantilever. © *2010 American Institute of Physics.*
[doi:10.1063/1.3482055]

I. INTRODUCTION

Breast tumors are known to exhibit a larger elastic modulus than the surrounding normal tissue under compression.[1–3] Potentially one can use elasticity measurement to detect breast tumor. However, the elastic modulus measurement is not adequate as benign breast tumors also exhibit a larger elastic modulus than the surrounding normal tissue.[2] Measuring tissue elastic modulus alone would not differentiate breast cancers from benign tumors. Anecdotal physicians' experience indicates that malignant tumors are less mobile than benign tumors. Although there are studies addressing the detection of breast tumors by using an indenter to monitor the stiffness contrast between the breast tumor and the surrounding healthy tissue,[4–7] very little quantitative information about breast cancer mobility is provided. In addition, these techniques monitor only the effective Young's modulus of the combined tissue and tumor system, thus providing limited or no information about the tumor modulus. Only a few studies have begun to investigate tumor mobility using complex ultrasound elastography analysis.[8,9]

On the other hand, it is also known that cancers generally exhibit more branching, interlocking, or spiculated interfaces with their surrounding tissue compared to benign tumors.[10–14] The notion that breast cancers are less mobile suggests that they behave differently from benign tumors under shear as shear involves movement of tissues in the lateral direction. The "immobility" of breast cancers indicates they are stiffer than benign tumors under shear. This difference may be due to the different interfacial properties between breast cancers and benign tumors. Currently, there are only a few studies examining the effect of stiffness of the tumor on the lateral movement of the probe[15] which can detect the hardness of the model tumor embedded in a matrix, resembling the healthy tissue. As far as the authors know there has been no study that examines the effect of tumor interfacial properties on their shear properties. It is of interest if one can correlate a tumor interfacial roughness with its shear property.

In this study, we examined the effect of interfacial roughness of model tumors on its behavior under shear both in terms of the degree and the direction of the interfacial roughness. The model smooth and rough tumors were constructed from modeling clay that exhibits a similar elastic modulus to breast tumors. Phantom breast tissues were constructed by embedding modeling-clay model tumors in gelatin that exhibited a similar elastic modulus to normal breast tissues. Gelatin has been extensively used as model breast tissues for elastography and ultrasound imaging for its similar viscoelastic behavior as breast tissues.[16–18] To address the effect of the degree of roughness, three-dimensional (3D) isotropic spiculated spheres resembling a spiky ball that had
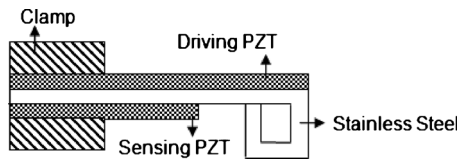
    81, 095104-1

FIG. 1. A schematic of the piezoelectric cantilever tissue elasticity sensor.

the same overall diameter but different spike lengths were constructed, which will be dubbed 3D model tumors hereafter. To address the directional effect, a rectangular block with corrugation in one direction that resembles a washboard was constructed, which we will dub one-dimensional (1D) model tumor hereafter. A completely smooth 1D model tumor was a rectangular block of the same overall dimensions and a completely smooth 3D model tumor was a sphere of the same diameter. In what follows, we will dub inclusions with a rough surface as R inclusions (R for rough) and inclusions with a smooth surface as S inclusions (S for smooth). The elastic modulus E and the shear modulus G of both S and R inclusions were measured by indentation tests[19–21] and by indentation shear test,[20,22] respectively, using a piezoelectric cantilever. For the direction effect, the shear measurements were carried out at various angles relative to the direction of corrugation. For the degree of roughness, the length of the spikes was varied relative to the overall diameter. The G/E ratio was used as a measure to correlate with surface roughness in terms of both degree of roughness and direction of roughness. In addition, the depth sensitivity of this G/E ratio measurement was also measured.

II. EXPERIMENTAL PROCEDURE

A. Piezoelectric cantilever

The piezoelectric cantilevers used in this study had a driving piezoelectric layer, lead zirconate titanate (PZT), on the top for force application and a shorter PZT layer at the bottom for displacement sensing as schematically shown in Fig. 1. Two cantilevers were used in this study. Cantilever A was 3.8 ± 0.2 mm wide with a 22 ± 0.2 mm long top PZT layer (T105-H4E-602, Piezo Systems Inc., Cambridge, MA) and a 11 ± 0.2 mm long bottom PZT layer bonded to a 50 μm thick stainless steel layer (Alfa Aesar, Ward Hill, MA) in the middle using a conductive epoxy (ITW Chemtorinics, Kennesaw, GA). Cantilever B was 8.0 ± 0.2 mm wide with a 25 ± 0.2 mm long top PZT layer and 11 ± 0.2 mm long bottom PZT layer bonded to a 50 μm thick stainless steel layer using a conductive epoxy. For both cantilevers A and B the square shaped tip was glued to the tip of the stainless steel using a nonconductive epoxy (Henkel Loctite Corporation, Industry, CA) and cured at room temperature for 1 day. Both the top and bottom PZT layers for cantilevers A and B were 127 μm thick. The top PZT layer was used for force application. When a voltage is applied across the thickness of the top PZT layer, it creates a lateral strain in the top PZT layer due to the converse piezoelectric effect of the top PZT layer which bends the cantilever. The force generated by the cantilever bending can be calibrated for force application.[20] The bottom PZT layer was used as a displacement meter. When the cantilever bends, a voltage difference is generated across the thickness of the bottom PZT layer due to the direct piezoelectric effect. The induced voltage across the bottom PZT layer can be used to measure the axial displacement of the cantilever. The square-shaped tip of the cantilever allows it to perform both compression and shear measurements using one single cantilever. Both of the cantilevers were clamped with a fixture made of 7.5 mm thick acrylic (McMaster-Carr, New Brunswick, NJ). The PZT layers had a piezoelectric coefficient, $d_{31} = -320$ pC/N, as specified by the vendor. The elastic modulus of the stainless steel and that of the PZT layers were 200 and 62 GPa, respectively, according to the vendors. The capacitance and the loss factor of a PZT layer were measured using an Agilent 4294 A impedance analyzer (Agilent, Palo Alto, CA). The contact area of the square stainless steel loop for cantilever A was 3.8×3.8 mm^2 and cantilever B was 8.0×8.0 mm^2. The effective spring constant K of the cantilever A was 143 N/m and B was 162.8 N/m as determined using the earlier published procedure.[20] A direct current (dc) power supply, HP E3631A (Hewlett-Packard Company, Palo Alto, CA), was used as the programmable dc voltage source. The measurements were conducted on a Newport optical table (RS1000, Newport Corporation, Irvine, CA) to minimize low-frequency background vibrations. The applied voltage across the driving PZT layer and the induced voltage across the sensing PZT layer were recorded on an Agilent Infiniium S4832D digital oscilloscope (Agilent, Palo Alto, CA). The dc power source and the oscilloscope were connected to a personal computer (PC). All voltage measurements, real-time elastic modulus computations, and data acquisitions were controlled from a PC by LABVIEW (National Instrument, Austin, TX) programming.

1. Model tissue with 1D model tumor

The model tissues were constructed by embedding modeling clay in gelatin (Fisher Scientific, Pittsburgh, PA). Three types of modeling clays were used. Modeling clay C54 (Play-Doh, Hasbro Ltd., Newport, UK) had an elastic modulus of 54 ± 12 kPa. Modeling clay C92 (Model Magic, Crayola, Easton, PA) had an elastic modulus of 92 ± 9 kPa, and modeling clay C145 (Modeling Clay, Crayola, Easton, PA) had an elastic modulus of 145 ± 10 kPa. Each type of modeling clay was made into two types of inclusions of the same size, 22 mm long, 12 mm wide, and 14 mm high but different surface textures: one with a smooth top surface, which we dub S inclusions [see Fig. 2(a)] and the other with a corrugated top surface, which we dub R inclusions (see Fig. 2(b)]. All R inclusions had rectangular grooves 2–4 mm wide and 7 mm deep running along the width of the inclusions. The concentration of the gelatin matrix was 0.07 g/ml prepared by mixing 19.25 g of gelatin (Fisher Scientific, Pittsburgh, PA) in 275 ml of water at 80 °C on a hot plate for 5 min, poured over the samples in the dish to the desired height, cooled at 5 °C for 1 h to solidify and then equilibrated at room temperature for 1 h prior to measurements.
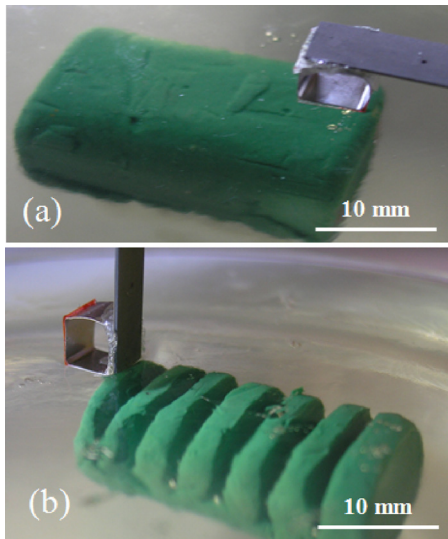
FIG. 2. (Color online) A photograph of (a) a smooth inclusion with the piezoelectric cantilever positioned for elastic modulus measurement and (b) a corrugated rough inclusion with the piezoelectric cantilever positioned for shear measurement perpendicular to the direction of the corrugation.

2. Model tissues with 3D isotropic inclusions

The 3D isotropic rough and smooth inclusions were made out of modeling clay C54. The photographs of 3D isotropic rough inclusions of various degrees of roughness are shown in Figs. 3(a)–3(d) and that of a 3D isotropic smooth inclusion is shown in Fig. 3(e). All 3D isotropic inclusions had an overall radius r approximately 14 ± 0.5 mm. The rough 3D inclusions were "spiky" balls each with a different average spike length s defined as the distance from the base of a spike to the tip of the spike as illustrated in Fig. 3(a). The average spike lengths for the rough inclusions shown in Fig. 3(a)–3(d) were 12 ± 0.5, 6 ± 0.5, 4 ± 0.5, and 2 ± 0.5 mm, respectively. The 3D smooth inclusion shown in Fig. 3(e) corresponded to a special case of the spiky balls with a zero spike length. The ratio of the spike length s to the overall radius of the inclusion may serve as a parameter to indicate the degree of roughness. For the inclusions shown in Figs. 3(a)–3(e), $s/r = 0.85$, 0.42, 0.28, 0.14, and 0, respectively. To create model tissues, these inclusions were suspended in gelatin with a concentration of 0.07 g/ml with similar procedure as described above. All the inclusions had a depth of 5 ± 1 mm as measured from the surface of the gelatin to the top of the inclusions.

B. Elastic modulus measurement

The elastic modulus as a function of position of a model tissue was measured using the piezoelectric cantilevers in the indentation mode[15] where the cantilever was parallel to the
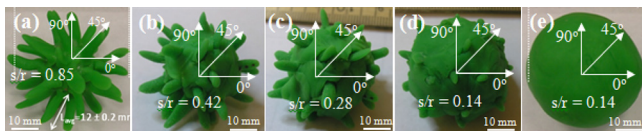

FIG. 3. (Color online) Photographs of 3D isotropic spiky-ball inclusions with a spike length s to overall radius r ratio. (a) $s/r = 0.85$, (b) $s/r = 0.42$, (c) $s/r = 0.28$, (d) $s/r = 0.14$, and (e) $s/r = 0$.

model tissue surface as shown in the photograph in Fig. 2(a). When a voltage V_a is applied to the top driving PZT layer of the cantilever, it generates a force which produces a vertical indentation displacement d to the tissue. The induced voltage V_{in} across the bottom sensing PZT layer is used to measure this tissue indentation electrically. The elastic modulus E of the tissue is related to the applied force F, the contact area A, and the vertical tissue indentation displacement d as[19,20]

$$E = \beta \left[\frac{1}{2} \left(\frac{\pi}{A} \right)^{1/2} (1 - \nu^2) \frac{F}{d} \right], \tag{1}$$

where ν is the Poisson's ratio of the tissue and β is an adjustable preconstant to account for the contact geometry. For a circular contact area, (i.e., a flat-ended cylindrical punch), $\beta = 1$.[23] For a rectangular contact area, $\beta = 1.01$.[24,25] Equation (1) for a circular contact area was derived by Sneddon from Boussinesq's solution for a flat-ended cylindrical punch on the surface of a half space.[23,24] Later King[25] showed that the result of using a square contact area differs only slightly (by 1%) from that of using a circular contact area, which is negligible compared to experimental uncertainty. The elastic modulus E deduced from Eq. (1) with $\beta = 1$ under indentation tests was validated within the experimental uncertainty by that measured by independent regular compression test of the same material in which the contact area equaled the sample area.[19,20] In the following, β will be approximated as unity and drop out of the subsequent expression in Eq. (2) for convenience. As the displacement d is linearly proportional to V_{in}, the elastic modulus E can be conveniently expressed in terms of V_{in} as[20,21]

$$E = \frac{1}{2} \left(\frac{\pi}{A} \right)^{1/2} (1 - \nu^2) \frac{K(V_{in,0} - V_{in})}{V_{in}}, \tag{2}$$

where K is the spring constant of the measuring cantilever and $V_{in,0}$ is the induced voltage across the sensing PZT layer of the measuring cantilever without the tissue. Thus, by knowing the $V_{in,0}$ beforehand and by measuring V_{in} on the tissue at various V_a, the elastic modulus E of the tissue can be deduced by plotting $(1/2)(\pi/A)^{1/2}(1 - \nu^2)K(V_{in,0} - V_{in})$ versus V_{in} and conveniently done through LABVIEW. The measurement detail can be found in Ref. 20.

C. Shear modulus measurement

The shear modulus as a function of the model tissue was measured using the indentation shear experiments where the cantilever was perpendicular to the tissue surface as shown in the photograph in Fig. 2(b). In this geometry, a force F parallel to the tissue surface is exerted on the tissue when a voltage V_a is applied to the driving PZT layer of the measuring cantilever, producing a horizontal displacement d to the tissue and an induced voltage V_{in} to the sensing PZT layer. The shear modulus G of the tissue can be empirically expressed in terms of the horizontal force F, the horizontal displacement d, and the contact area A as[20]
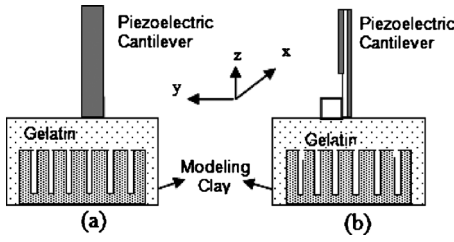
FIG. 4. A schematic of the shear (a) being parallel to the direction of corrugation (x direction) and (b) being perpendicular to the corrugation (y direction).

$$G = \alpha \frac{1}{2}\left(\frac{\pi}{A}\right)^{1/2}(1-\nu^2)\frac{F}{d}, \quad (3)$$

where α is a constant to be determined empirically. Note that presently, there is no known analytic expression that relates the shear modulus, the lateral force F, and the lateral displacement d on the surface within the contact. Equation (3) was purely empirical as reflected by the adjustable preconstant α in the front of Eq. (3) that is to be fitted experimentally. The shear modulus of a material deduced by Eq. (3) under indentation shear was validated by that deduced from independent regular shear measurements on the same material in which the contact area equaled the sample area and α in Eq. (3) was found to be 1 ± 0.2.[20] These earlier results demonstrated that within the experimental uncertainty, Eq. (3) was adequate in deducing the shear modulus from an indentation shear test. As theoretical derivation of the expression for the shear modulus under indentation shear is not within the scope of this study, in the following we will use Eq. (3) to deduce the shear modulus. Furthermore, α will be approximated as unity and drop out of the subsequent expression of Eq. (4) for convenience. Because the induced voltage of the sensing PZT layer is proportional to the horizontal displacement of the tissue, similarly, the shear modulus G can be deduced using the induced voltage simply as[20]

$$G = \frac{1}{2}\left(\frac{\pi}{A}\right)^{1/2}(1-\nu^2)\frac{K(V_{in,0}-V_{in})}{V_{in}} \quad (4)$$

which can be obtained by measuring V_{in} and plotting $(1/2) \times (\pi/A)^{1/2}(1-\nu^2)K(V_{in,0}-V_{in})$ versus V_{in} using LABVIEW.

III. RESULTS AND DISCUSSIONS

A. Probing 1D anisotropic inclusions

Experiments were carried out on smooth (S) inclusions and corrugated or rough (R) inclusions made out of model clay C54, C92, and C145 as described above with a 3 ± 1 mm depth where the depth of an inclusion was defined as the distance from the gelatin surface to the top of the inclusion. For the shear measurement, the displacement can be either parallel to the corrugation (i.e., the displacement is in the x direction) as schematically shown in Fig. 4(a) or perpendicular to the corrugation (i.e., the displacement is in the y direction) as schematically shown in Fig. 4(b) [also see the photograph in Fig. 2(b)]. Conceivably, there may be difference in these two measurements on the corrugated inclusions. Therefore, the shear modulus was measured both with the contact area moving parallel to [Fig. 4(a)] and perpen-
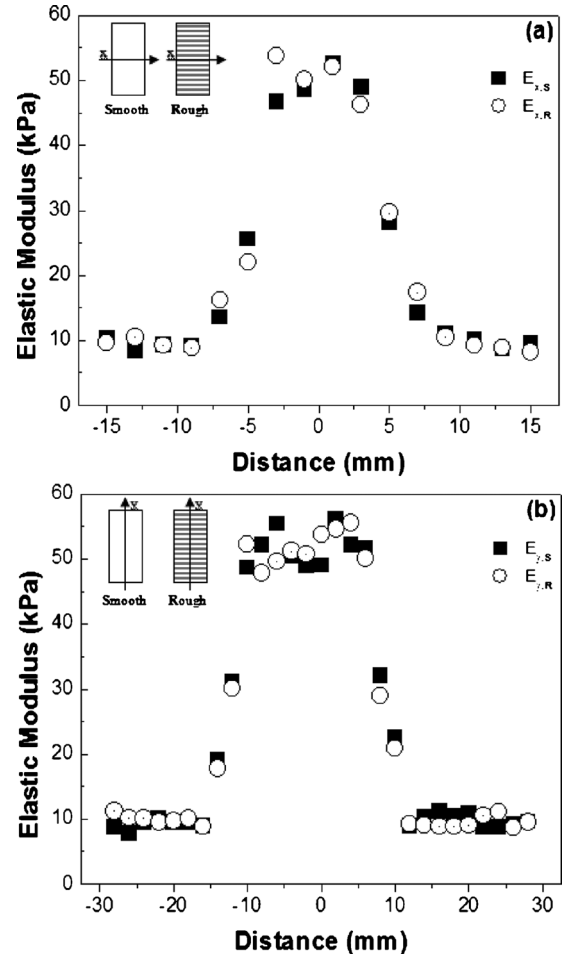

FIG. 5. Elastic modulus vs distance from the center of the inclusion in (a) x direction and (b) y direction for the smooth (full squares) and rough (open circles) inclusions made of C145.

dicular to [Fig. 4(b)] the corrugation. Since the corrugation was in the x direction [see Figs. 4(a) and 4(b)], we will call the shear modulus measured with the contact area moving parallel to the corrugation as G_x and that measured with the contact area perpendicular to the corrugation as G_y. Similarly, G_x and G_y are also measured over the S inclusions. Meanwhile, the elastic moduli of each inclusion obtained scanning along the x and y directions are termed E_x and E_y, respectively. Note that all the S inclusions and R inclusions had the same length, width, and height except that the S inclusions had a smooth top surface and the R inclusions a corrugated surface. The scanned area for each inclusion and its vicinity was 44×68 mm^2 with a 4 mm interval.

As an example, the elastic modulus profiles in the x direction [see the inset in Fig. 5(a)] and those in the y direction [see the inset in Fig. 5(b)] of the S and R inclusions made of the C145 modeling clay are shown in Figs. 5(a) and 5(b), respectively. Shown in Figs. 5(a) and 5(b) are the elastic modulus profiles, $E_{x,S}$, $E_{x,R}$, $E_{y,S}$, and $E_{y,R}$, where $E_{x,S}$ and $E_{x,R}$ are the elastic modulus of the S and R inclusions, respectively, scanned along the x direction along the center line of the inclusions, as schematically shown in inset in Fig. 5(a). $E_{y,S}$ and $E_{y,R}$ are the elastic modulus of the S and R inclusions, respectively, along the y direction along the center line of the inclusions, as schematically shown in inset in
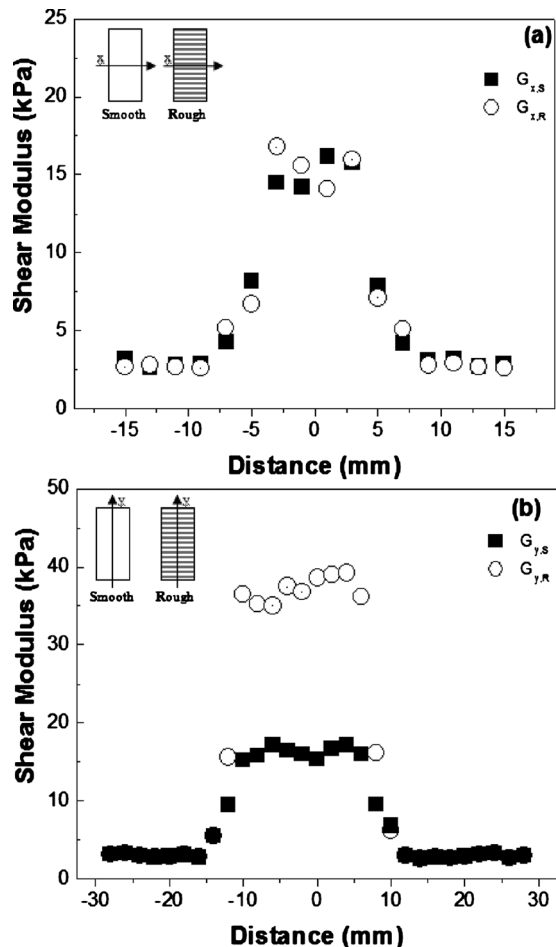
FIG. 6. Shear modulus vs distance from the center of the inclusion in (a) x direction and (b) y direction for the smooth (full squares) and rough (open circles) inclusions made of C145.

Fig. 5(b). Clearly, $E_{x,S}$, $E_{x,R}$, $E_{y,S}$, and $E_{y,R}$ were all about 52 ± 3 kPa above the inclusions and dropped to a constant value of about 9 ± 1 kPa away from the inclusions, indicating that the elastic modulus measurement was independent of the surface roughness and scan direction. The constant value of about 9 ± 1 kPa away from the inclusions was the elastic modulus of the gelatin matrix. Meanwhile the length and width of the model tumors could be estimated from the width at half the peak height, which gave a length of 19 ± 1 and 20 ± 1 mm and a width of 9 ± 1 and 9.4 ± 1 mm for the S and R inclusions, respectively, in agreement with the known lengths and widths of the S and R inclusions. The shear modulus profile in the x direction [see the inset in Fig. 6(a)] and that in the y direction [see the inset in Fig. 6(b)] are shown in Figs. 6(a) and 6(b), respectively, where $G_{x,S}$ and $G_{x,R}$ were the shear moduli of the S and R inclusions measured with the shear motion along the x direction (parallel to the corrugation of the R inclusions) along the center line of the inclusions, respectively, as schematically shown in inset in Fig. 6(a). $G_{y,S}$ and $G_{y,R}$ were the shear moduli of the S and R inclusions measured with the shear motion along the y direction (perpendicular to the corrugation of the R inclusions) along the center line of the inclusions, respectively, as schematically shown in inset in Fig. 6(b). For the S inclusion, both $G_{x,S}$ and $G_{y,S}$ were about 16 ± 1 kPa above the inclu-

sion independent of the shear direction and fell off to about 3 ± 1 kPa away from the inclusion. In contrast, for the R inclusion, the shear modulus measured perpendicular to the corrugation, $G_{y,R}$, was 37 ± 2 kPa above the inclusion whereas the shear modulus measured parallel to the corrugation, $G_{x,R}$, was about 16 ± 1 kPa. The length and width of the S and R inclusions as estimated from the width at half the peak height was 19.2 ± 1 and 19.8 ± 1 mm, 9.8 ± 1 and 9.6 ± 1 mm, respectively, in agreement with those obtained from the elastic modulus profiles and with the known values. Away from the inclusion both $G_{y,R}$ and $G_{x,R}$ fell off to a constant value of about 3 ± 1 kPa. The above results indicate that surface roughness plays a role in the shear modulus measurements above the inclusion. When the shear motion was parallel to the direction of corrugation, the measured shear modulus of a corrugated inclusion was similar to that of a smooth inclusion. On the other hand, when the shear motion was perpendicular to the direction of corrugation, the measured shear modulus was more than twice that of a smooth inclusion. Finally, the constant value of about 3 ± 0.5 kPa in $G_{y,S}$, $G_{y,S}$, $G_{x,S}$ and $G_{x,R}$ away from the inclusions corresponded to the shear modulus of the gelatin matrix.

1. G/E ratios

It is known that Poisson's ratio ν of an isotropic tissue or soft material is 0.5, which gives a shear modulus (G) to elastic modulus (E) ratio G/E of about 0.3. We plot $G_{x,S}/E_{x,S}$ and $G_{x,R}/E_{x,R}$ in Fig. 7(a) for the S and R inclusions scanned in x direction and $G_{y,S}/E_{y,S}$ and $G_{y,R}/E_{y,R}$ in Fig. 7(b) for the S and R inclusions scanned in y direction, as shown schematically in the insets in Figs. 7(a) and 7(b). Note that Figs. 7(a) and 7(b) include the results from the S and R inclusions made from all three different modeling clays: C54, C92, and C145. From Fig. 7(a) we can see that for all the S and R inclusions, the G/E ratio remained around 0.3 above or away from the inclusions in the x direction. From Fig. 7(b), the G/E ratio of the S inclusions in the y direction ($G_{y,R}/E_{y,R}$) remained around 0.3 above or away from the inclusion, while the G/E ratio of the R inclusions in the y direction ($G_{y,R}/E_{y,R}$) was larger than 0.7 above the inclusion when the shear measurement was perpendicular to the direction of corrugation and fell off to about 0.3 away from the inclusion. As can be seen, the enhanced shear modulus of the R inclusions measured perpendicular to the corrugation translated to an enhanced G/E ratio much larger than the 0.3 expected of isotropic soft tissues.

2. Effect of orientation of corrugation

It is interesting that in the present model tissues, the shear modulus G measured perpendicular to the direction of corrugation was more than twice that measured parallel to the corrugation or that measured over a smooth inclusion. As a result, the shear modulus to elastic modulus ratio G/E was enhanced to over 0.7 above a rough inclusion when measured perpendicular to the corrugation in contrast to the G/E ratio of a smooth inclusion or that of a rough inclusion measured parallel to the corrugation. We speculate that the enhanced shear modulus and hence the enhanced G/E ratio
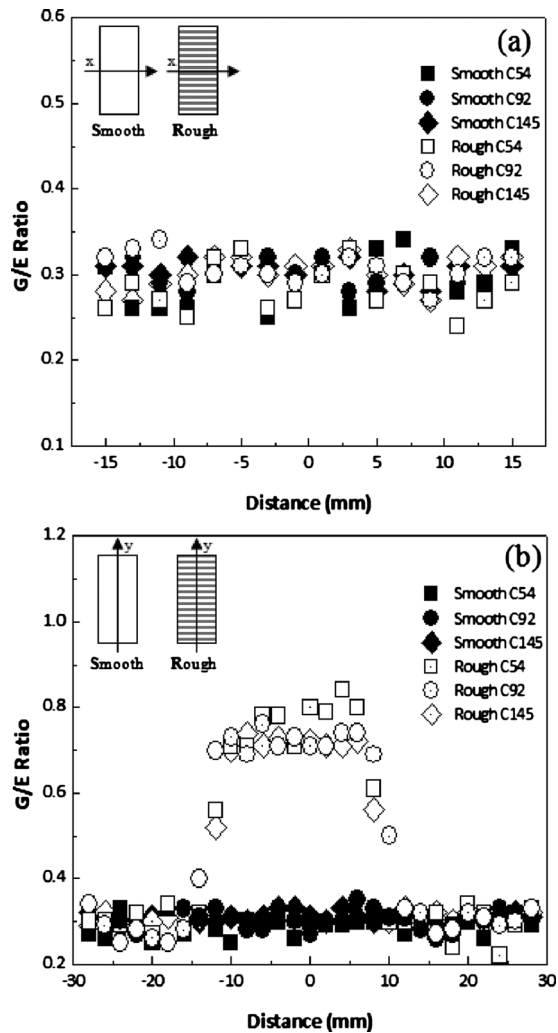
FIG. 7. G/E ratio of smooth (full data points) and the rough (open data points) inclusions made of C54, C92, and C145 (a) in the x direction and (b) in the y direction.

FIG. 8. (a) G/E ratio vs distance and (b) G/E ratio vs scanning angle for the smooth and rough inclusions scanned at different angles.

over a rough inclusion when measured perpendicular to the direction of corrugation was due to the interlocking nature of the corrugated surface which made it harder for either the gelatin or the modeling clay to move horizontally when subject to a shear stress.

To further investigate how the G/E ratio changes with the orientation of the corrugation, we measured the E and G along a path that had an angle θ with the x axis as schematically shown in the inset of Fig. 8(a). The obtained G/E versus distance from the center of the inclusion at various θ is shown Fig. 8(a). As can be seen, the G/E ratio over the rough inclusion progressively increased from 0.33 for $\theta = 0°$ (parallel to corrugation) to above 0.7 for $\theta = 90°$ (perpendicular to corrugation) whereas for the smooth inclusion the G/E ratio remained around 0.33 regardless of the angle and whether it was above the inclusion or the gelatin. In Fig. 8(b), we plot the G/E over the inclusion versus the scanning angle. As can be seen, for the smooth inclusion, the G/E remained around 0.3 while that over the rough inclusion increased with the scanning angle. This clearly indicates that the direction of the corrugation had a direct effect on the G/E ratio and that the G/E increased progressively from
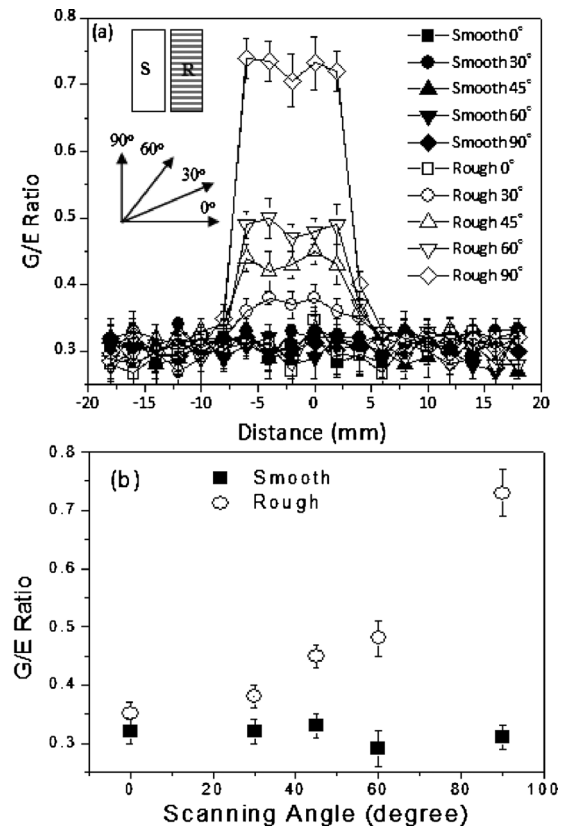
0.33 when the shear was parallel to the corrugation to above 0.7 when the shear was perpendicular to the corrugation.

It is also worth noting that the present contact size was 3.8 mm which was larger than the groove width, 2 mm. Therefore, most likely, in most measurements, the contact area either covered only a modeling-clay tooth or part of a modeling-clay tooth and part of a groove. Under such conditions, the depth of the R inclusion was essentially the depth of the modeling-clay teeth, which were what we used for comparison in this study. However, if the contact size were smaller than the groove size, the measured shear modulus may differ depending on whether the measurement was above a modeling clay tooth either partially or completely or entirely above a groove. The shear modulus measured above a modeling-clay tooth would be similar to what we measured in this study whereas that measured above a groove may be different as the groove had a much large depth than the modeling-clay teeth. While these questions are of interest they are not within the scope of this study, we will address these questions in a future publication.

B. Probing 3D isotropic inclusions

All 3D isotropic inclusions were scanned using indentation and indentation shear experiments, along 0°, 45°, and 90°, as shown in Figs. 3(a)–3(e). The results of the indentation and indentation shear scans of 3D isotropic inclusions with a depth of 5 ± 1 mm embedded in gelatin were scanned along the 0° are shown in Figs. 9(a) and 9(b), respectively. As shown in Fig. 9(a) inclusions with all s/r ratios exhibited
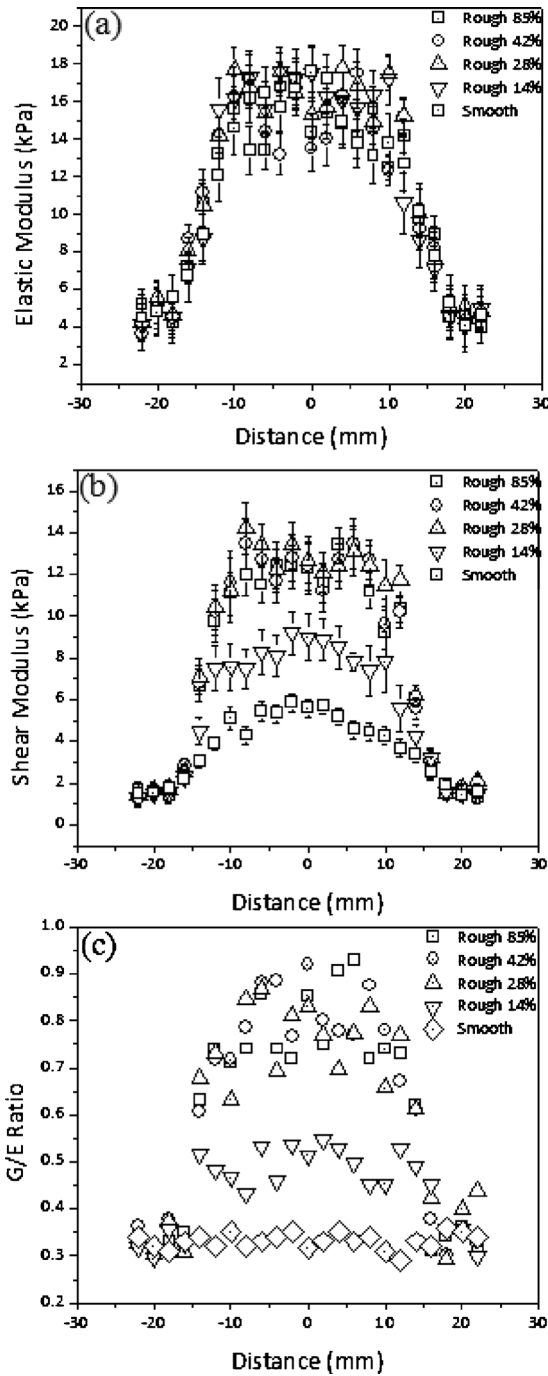
FIG. 9. (a) Elastic modulus, (b) shear modulus, and (c) G/E ratio vs distance from the center of the inclusion in x direction for the 85%, 42%, 28%, and 14% s/r ratio of rough inclusion and smooth inclusion.

FIG. 10. G/E ratio vs s/r ratio of the 5%, 42%, 28%, and 14% s/r ratio of rough inclusion and smooth inclusion. The C ratio (C) results are labeled on top of each data point, where C ratio is as defined in the text.

inclusion with $s/r = 0.14$, the G/E value increased to about 0.5 above the inclusions. For inclusions with $s/r = 0.28$, 0.42, and 0.85, the G/E values were all higher than 0.7 above the inclusion. In Fig. 10, we plot the G/E value above the inclusion versus the value of s/r. Clearly the G/E value of the inclusion depended on the degree of roughness. For the present model, all inclusions with an s/r ratio larger than 0.28 exhibited a G/E larger than 0.7.

Similar E and G scans were carried out at 45° and 90° relative to the x axis as schematically shown in Figs. 3(a)–3(e). Table I summarizes the G/E ratio over all the isotropic inclusions when scanned at 0°, 45°, and 90° relative to the x axis. As can be seen, for all 3D inclusions, the values obtained for G/E were essentially the same for all three directions as expected of isotropic inclusions.

As breast cancers are known to be more spiculated than benign tumors, there have been mathematical models proposed to analyze lesions found in mammography and ultra-

an elastic modulus in tight band ranging from 14 to 18 kPa. In comparison, Fig. 9(b) shows that inclusions with $s/r = 0.85$, 042, and 0.28 exhibited a shear modulus of about 12–14 kPa while the inclusion with $s/r = 0.14$ exhibited a shear modulus of 8–9 kPa above the inclusion and the inclusion with s/r exhibited a shear modulus of about 5–6 kPa over the inclusion as measured by using the 8.0 ± 0.5 mm wide piezoelectric cantilever. In Fig. 9(c), we plot the G/E versus distance along the 0°. As can be seen, for the smooth inclusion ($s/r = 0$), the G/E remained around 0.3 regardless it is away from the inclusion or over the inclusion. For the
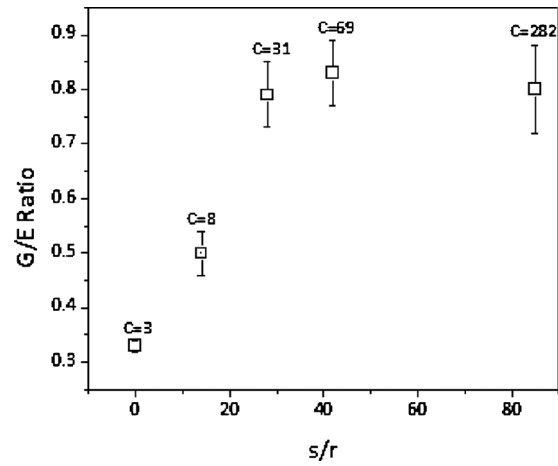
TABLE I. G/E values of 3D isotropic spiky-ball inclusions with various length s to overall radius r ratios scanned at 0°, 45°, and 90° relative to the x-axis as schematically shown in Figs. 3(a)–3(e) where G and E are the shear modulus and elastic modulus measured over the inclusions.

s/r	θ (deg)	G/E
0.85	0	0.80 ± 0.08
	45	0.76 ± 0.09
	90	0.87 ± 0.08
0.42	0	0.83 ± 0.06
	45	0.77 ± 0.10
	90	0.78 ± 0.11
0.28	0	0.79 ± 0.06
	45	0.78 ± 0.05
	90	0.74 ± 0.08
0.14	0	0.50 ± 0.04
	45	0.45 ± 0.06
	90	0.51 ± 0.03
0	0	0.33 ± 0.01
	45	0.32 ± 0.03
	90	0.34 ± 0.03

TABLE II. Depth of the smooth (S) and rough (R) inclusions inside the gelatin.

S inclusion number	R inclusion number	Depth (mm)
1	1	1.7
2	2	3
3	3	4.7
4	4	7
5	5	8.6
6	6	10.1
7	7	11.6

sound to discern its malignancy. One of the models is to compute the circularity C of the tumor where $C=P^2/4A$ with P being the perimeter and A being the area of the tumor in the image.[10] It was shown that malignant tumors exhibited C larger than 20 while benign tumors exhibit smaller C.[10] For comparison, we measured the perimeters and areas of the two-dimensional projection images of all the isotropic inclusions and computed the circularity C. The obtained C was labeled on the top of the data points in Fig. 10. As can be seen, for inclusions that exhibited a G/E larger than 0.7, i.e., inclusions with a $s/r=0.28$, 0.42, and 0.85, the values of C were larger than 20 and for the inclusions whose G/E were less than 0.7, i.e., inclusions with a $s/r=0$, and 0.13, the values of were much smaller than 20. This comparison is interesting and encourages further comparison of the G/E ratios with more surface roughness models in the future.

C. Depth sensitivity of *G/E* ratio measurements

The present elastic modulus and shear modulus measurements using the piezoelectric cantilever approach relies on the contact of the piezoelectric cantilever with only one surface of the sample. The advantage of such one contact approach is the ability/potential to do *in vivo* measurement. The drawback is that tissue below a certain depth may not be affected by such one-finite-contact measurements thus may not be measurable. It is desirable to know how deep underneath the surface the present G/E ratio measurement is valid. Since the G/E ratio involved both E and G measurements, it is necessary to determine the depth sensitivity of G and E separately before one can determine that of G/E. The depth sensitivity of E by the present piezoelectric cantilever has been characterized and shown to be twice the size of the contact area[13] previously where the depth sensitivity is defined as the maximum depth within which the measurement was valid. In this study, we examined the depth limit of the shear modulus measurement using seven smooth inclusions and seven corrugated rough inclusions, each 22 mm long and 12 mm wide, made of C92 modeling clay with various heights (and therefore various depths) embedded in gelatin. The depths of the seven S inclusions and seven R inclusions are listed in Table II. As mentioned above, C92 modeling clay was chosen for this model study because it has an elastic modulus that is closer to breast tumors. The gelatin used in this experiment had an elastic modulus of 3 ± 0.2 kPa and shear modulus of 1 ± 0.2 kPa as determined on a separate gelatin sample prepared in the same manner. The elastic
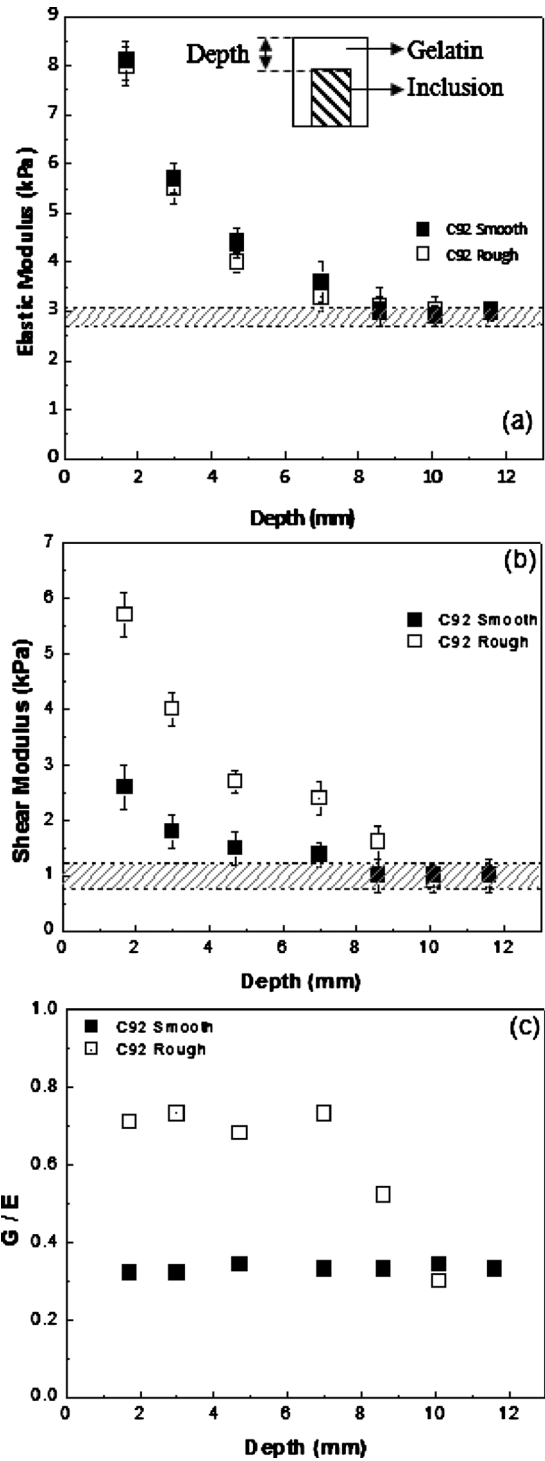

FIG. 11. (a) Elastic modulus, (b) shear modulus, and (c) G/E vs inclusion depth of rough and smooth inclusions made of C92. The depth of the inclusion is schematically shown in the inset in (a).

moduli and shear moduli of the seven smooth (S) inclusions and seven corrugated rough (R) inclusions were measured above the centers of the inclusions and the shear moduli of the rough inclusions were measured perpendicular to the direction of corrugation. In Fig. 11(a), we plot the resultant elastic modulus versus inclusion depth for both the S inclusions (full squares) and the R inclusions (open squares) where the inclusion depth is defined as the distance from the gelatin surface to the top of the inclusion as schematically

shown in the figure inset of Fig. 11(a). The shaded horizontal band as shown in Fig. 11(a) represents the elastic modulus of the gelatin matrix within the experimental uncertainty. Empirically, the depth sensitivity of the elastic modulus measurement was determined as the depth at which the measured elastic modulus of an inclusion became indistinguishable from that of the gelatin matrix. As can be seen, the measured elastic modulus versus depth of the S inclusions agreed with that of the R inclusions, both exhibiting depth sensitivity between 7 and 8 mm, about twice the width of the cantilever, 3.8 mm, in agreement with the published results.[13] In Fig. 11(b), we plot the measured shear modulus versus depth for the S inclusions (full squares) and the R inclusions (open squares). The shaded horizontal band indicated the value of the shear modulus of the gelatin matrix with its standard deviation. As can be seen, the depth sensitivity for the shear modulus of the S inclusions and that of the R inclusion were also around 8 mm as similar to that of the elastic modulus. In Fig. 11(c), we plot G/E versus inclusion depth for both the S inclusions (full squares) and the R inclusions (open squares). For the S inclusions, the G/E ratio remained around 0.3 as expected for all depths. For the R inclusions, the G/E remained around 0.7 for depths smaller than 8 mm and the value of G/E decreased when the depth became larger than 8 mm and became 0.3 when the depths were larger than 10 mm. From Fig. 11(c), one can conclude the depth sensitivity of the present 3.8 mm wide cantilever was around 8 mm, about twice the size of the contact area (which was width of the cantilever) as similar to the depth sensitivity of individual elastic modulus and shear modulus measurements.

IV. CONCLUSIONS

In this study, we have examined the effect of an inclusion's interfacial roughness with its matrix to the ratio of the effective shear modulus to the effective elastic modulus measured over the inclusion by indentation and indentation shear measurements using piezoelectric cantilevers. Two types of surface roughness have been investigated: 1D anisotropic corrugated inclusions and 3D isotropic spiky-ball inclusions. We showed that for both the 1D anisotropic corrugated inclusions and the 3D isotropic spiky-ball inclusions, the G/E ratio was larger than 0.7 while the smooth inclusions exhibited a G/E of about 0.3. We further showed that for the 1D corrugated inclusions, the G/E ratio depends on the direction of the shear relative to corrugation. For an angle of less than 60° between the direction of shear and corrugation, the G/E ratio is less than 0.5 and decreased with a decreasing angle. For 3D isotropic spiky-ball inclusions, the G/E ratio of the

inclusion depends on the degree of roughness which can be described by the ratio of the spike length to the overall radius, s/r. We showed that for inclusions with an s/r ratio larger than or equal to 0.28, the G/E over the inclusions were larger than 0.7. It is also of interest to note that an s/r ratio larger than 0.28 corresponded to circularity larger than 20. In addition, we showed that the depth limit that a piezoelectric cantilever can probe the G/E of an inclusion was thrice the width of the size of the probe area of the piezoelectric cantilever.

[1] J. F. Greenleaf, M. Fatemi, and M. Insana, Annu. Rev. Biomed. Eng. **5**, 57 (2003).
[2] A. Samani, J. Zubovits, and D. Plewes, Phys. Med. Biol. **52**, 1565 (2007).
[3] P. S. Wellman, E. P. Dalton, D. Krag, K. A. Kern, and R. Howe, Arch. Surg. **136**, 204 (2001).
[4] A. M. Zimmerman, N. A. Langrana, and S. M. Dunn, Proceedings of the ASME Bioengineering Conference, 2001, Vol. 50, p. 1.
[5] W. Yu, Y. Li, Y. P. Zheng, N. Y. Lim, M. H. Lu, and J. Fan, Meas. Sci. Technol. **17**, 1785 (2006).
[6] J. P. A. Arokoski, J. Surakka, T. Ojala, P. Kolari, and J. S. Jurvelin, Physiol. Meas **26**, 215 (2005).
[7] E. Samur, M. Sedef, C. Basdogan, L. Avtan, and O. Duzgun, Med. Image Anal. **11**, 361 (2007).
[8] E. E. Konofagou, T. Harrigan, and J. Ophir, Ultrasonics **38**, 400 (2000).
[9] E. Chen, Ph.D. thesis, University of Illinois at Urbana-Champaign, 1995.
[10] K. Kim, J. Kim, and B. Min, J. Digit Imaging **15**, 224 (2002).
[11] S. Orel, N. Kay, C. Reynolds, and D. C. Sullivan, Radiology **211**, 845 (1999).
[12] S. F. Huang, R. F. Chang, D. R. Chen, and W. K. Moon, IEEE Trans. Med. Imaging **23**, 111 (2004).
[13] C. Varela, S. Timp, and N. Karssemeijer, Phys. Med. Biol. **51**, 425 (2006).
[14] I.-S. Jung, D. Thapa, and G.-N. Wang, Lect. Notes Comput. Sci. **3614**, 1079 (2005).
[15] P. Yen, D. Chen, K. Yeh, and P. Chu, Med. Eng. Phys. **30**, 1013 (2008).
[16] K. Ishida, Y. Hayakawa, K. Tsuji, H. Doi, M. Kaitoo, and M. Nakamura, IFMBE Proc. **14**, 1426 (2007).
[17] L. Han, N. J. Alison, and B. Michael, Ultrasound Med. Biol. **29**, 813 (2003).
[18] T. J. Hall, M. Bilgen, and M. F. Insana, IEEE Trans. Ultrason. Ferroelectr. Freq. Control **44**, 1355 (1997).
[19] S. T. Szewczyk, W. Y. Shih, and W.-H. Shih, Rev. Sci. Instrum. **77**, 044302 (2006).
[20] H. O. Yegingil, W. Y. Shih, and W.-H. Shih, J. Appl. Phys. **101**, 054510 (2007).
[21] H. O. Yegingil, W. Y. Shih, and W.-H. Shih, Rev. Sci. Instrum. **78**, 115101 (2007).
[22] A. Markidou, W. Y. Shih, and W.-H. Shih, Rev. Sci. Instrum. **76**, 064302 (2005).
[23] I. N. Sneddon, Int. J. Eng. Sci. **3**, 47 (1965).
[24] G. M. Pharr, W. C. Oliver, and F. R. Brotzen, J. Mater. Res. **7**, 615 (1992).
[25] R. B. King, Int. J. Solids Struct. **23**, 1657 (1987).